Composites Part B 326 (2026) 114057

Contents lists available at ScienceDirect

Composites Part B

journal homepage: www.elsevier.com/locate/composites

2D bio-inspired reinforcement mesh for toughening composite bonded joints: Effect of orientation and adhesion patterning

Zhiyuan Xu [a,b], Ran Tao [a], Sofia Teixeira de Freitas [a,c,*]

[a] Faculty of Aerospace Engineering, Delft University of Technology, Delft 2629 HS, Netherlands
[b] CCCC Guangdong-Hong Kong-Macao Greater Bay Area Innovation Research Institute, China
[c] IDMEC, Instituto Superior Técnico, Universidade de Lisboa, Lisboa, Portugal

ARTICLE INFO

Keywords:
Filament bridging
Biomimetic materials
X-ray
Orientation effect
Crack bifurcation

ABSTRACT

Inspired by the sacrificial bonds and hidden lengths mechanism found on the molecular structure of spider silk, this study investigates a bio-inspired overlapping curl (OC) 2D-mesh fabricated via 3D-printing and integrated into the adhesive layer as a reinforcement architecture. Mode I double cantilever beam tests were conducted to investigate the effects of mesh orientation (0° and 45°) and adhesion patterning on crack propagation and fracture toughening. The results show that the 2D-OC mesh itself effectively activates extensive filament bridging, leading to an apparent energy release rate (ERR) enhancement up to 47 %. In contrast, adhesion patterning partially suppresses bridging. X-ray computed tomography and fracture surface analyses further reveal that reinforcement orientation governs crack front evolution and bridging activation. In particular, the 45°-oriented mesh induces a zig-zag crack front that promotes crack deflection and bifurcation, thereby activating more bridging filaments than the 0°-oriented configuration. Based on these observations, a coupled toughening framework is established, linking the apparent ERR enhancement to the combined effects of adhesion patterning width, reinforcement orientation, bridging activation, and filament material behavior. The findings provide mechanistic insight into crack–reinforcement interactions and offer design guidelines for architected bio-inspired reinforcements in adhesively bonded composite structures.

1. Introduction

Carbon fiber reinforced polymer (CFRP) adhesively bonded joints have been a promising joining technology in lightweight structural applications due to their high design flexibility and compatibility with multi-material systems [1–3]. Compared with traditional mechanical fastening (e.g., bolts and rivets), adhesive bonding enables improved uniform load transfer and reduced stress concentrations [4,5]. Nevertheless, the fracture resistance of adhesive joints remains a critical concern, as the thermoset epoxy adhesives often exhibit brittle failure and are highly susceptible to crack propagation [6,7]. To broaden the application of the adhesively bonded joints, extensive studies have focused on enhancing joint fracture toughness through multiscale toughening strategies, such as the addition of nano- or micro-reinforcements (e.g., carbon nano tubes and graphene) [8,9], corrugated substrate [10,11], and substrate surface adhesion engineering [12–15]. These approaches generally improve fracture resistance by enhancing matrix toughness, increasing crack path tortuosity, or strengthening interfacial adhesion. However, their toughening efficiency is often constrained by limited crack bridging capability or by the complexity of manufacturing and surface treatment.

Apart from these toughening strategies, introducing bridging elements into the bonded joints has attracted considerable attention as an effective extrinsic approach. One representative example involves inserting through-thickness Z-pins into composite bonded joints [16], where crack growth can be inhibited through additional energy dissipation by Z-pins pull-out. However, Z-pins can induce stress concentrations in the substrate and increase the risk of fiber breakage due to fiber waviness [17], thereby compromising the in-plane mechanical performance. As an alternative, architecting the adhesive layer with crack-arresting reinforcement elements provides a more flexible solution. Integrated reinforcements can be broadly categorized according to their geometric form into one-dimensional (1D) and two-dimensional (2D) architectures. For 1D reinforcement, examples include natural and synthetic fibers inserted into the adhesive layer [6,7,18]. In terms of 2D reinforcement, mesh-type structures have also been explored [19–23]. Maloney et al. [22] introduced a copper mesh into the adhesive layer, enhancing the fracture resistance by 60 % but at the cost of increasing

* Corresponding author at: Faculty of Aerospace Engineering, Delft University of Technology, Delft 2629 HS, Netherlands.
E-mail address: s.teixeiradefreitas@tudelft.nl (S. Teixeira de Freitas).

https://doi.org/10.1016/j.compositesb.2026.114057
Received 5 July 2026; Received in revised form 3 August 2026; Accepted 3 August 2026
Available online 8 August 2026

joint thickness and weight. Yudhanto et al. [23] reported a 4 times increase in mode I fracture toughness by incorporating a polyamide mesh, which enhanced energy dissipation through progressive filament deformation, stretching, and pull-out. However, the observed improvement was highly sensitive to void content, resulting in unstable crack propagation.

In summary, incorporating second-phase reinforcements into the adhesive layer has emerged as a promising extrinsic toughening strategy. Despite their differences in geometry and material composition, most of these reinforcement systems derive their toughening effect from filament bridging through deformation, pull-out, or crack-arrest mechanisms. The effectiveness of such approaches, therefore, depends not only on the presence of reinforcement elements but also on their successful engagement by the propagating crack front. Previous studies have attempted to address this issue by guiding crack paths through adhesion patterning to enforce crack–reinforcement interaction [22,24], or by increasing filament waviness to promote bridging activation [23]. Nevertheless, the resulting fracture response remains highly sensitive to the geometric architecture, spatial distribution, and orientation of the reinforcement. These parameters collectively govern where and when the reinforcement is engaged, as well as whether stable and sustained filament bridging can be established during crack propagation. Therefore, the deliberate control of crack evolution and bridging activation through reinforcement architecture remains insufficiently understood.

Through billions of years of evolution, biological materials have evolved highly efficient hierarchical architectures with remarkable mechanical performance [25,26], providing valuable inspiration for the design of advanced reinforcement systems. Spider webs, evolved over four million years [27], exhibit remarkable energy absorption when capturing flying prey, as shown in Fig. 1(a). At the molecular-scale, the exceptional toughness of spider silk originates from the hierarchical organization of its semi-amorphous domains interconnected by hydrogen bonds. Under loading, hydrogen bonds rupture first, acting as sacrificial bonds, while the helical semi-amorphous domains progressively unfold, releasing hidden length and gradually transforming into a more aligned and tensioned configuration. This sacrificial bonds and hidden lengths (SBHL) mechanism enables controlled energy dissipation, progressive deformation, and enhanced damage tolerance achieved through structural architecture rather than material stiffness alone. As illustrated in Fig. 1(a), the present overlapping curl (OC) reinforcement is developed through an engineering translation of the SBHL mechanism from the molecular to the structural scale. Rather than reproducing the morphology of spider webs, the OC architecture preserves the functional sequence of the SBHL mechanism. Specifically, the helical curls act as engineered hidden lengths that progressively unfold during crack propagation, while the progressive engagement and unfolding of individual OC filaments enable sustained energy dissipation through filament bridging, analogous to the gradual release of hidden lengths initiated by sacrificial bond rupture in spider silk. Based on this engineering concept, bio-inspired OC reinforcements have been fabricated via 3D-printing and integrated into elastomer and epoxy matrices, demonstrating enhanced impact and fracture resistance, respectively [28–30]. In adhesively bonded composite joints, our previous work [24] demonstrated that 1D OC filaments could be activated by adhesion patterning-induced crack deflection, thereby increasing fracture resistance. However, their bridging effect remained localized and strongly dependent on whether the propagating crack engaged individual filaments. Extending the OC concept to a 2D mesh introduces multiple crack–reinforcement interaction sites, with the potential to promote more extensive and sustained filament bridging. However, the governing conditions for their bridging activation and crack–reinforcement interaction are yet to be established.

This study, mimicking the SBHL toughening mechanism of spider silk, introduces the bio-inspired 2D overlapping curl mesh reinforcement integrated into the adhesive layer of CFRP bonded joints. Polyamide 6 overlapping curls are fabricated via 3D-printing and arranged in a dense 2D mesh architecture, in contrast to previously reported 1D fiber reinforcements [7,24]. Through the combination of macroscopic fracture testing, in-situ imaging, fracture surface analysis, and three-dimensional X-ray computed tomography, this work aims to elucidate the underlying crack–reinforcement interaction mechanisms and establishes practical design principles for bio-inspired reinforcement strategies in composite bonded joints.

2. Materials and methods

2.1. Materials

The double cantilever beam (DCB) substrate was manufactured from unidirectional carbon fiber prepregs Hexply 8552 – IM7 toughened epoxy resin (Hexcel Composites, Cambridge, UK). In order to manufacture the CFRP substrates, eight plies of the CFRP prepreg were stacked by hand layup in the 0-degree direction. The CFRP laminates were then cured in an autoclave on a flat aluminum plate under 7 bars of pressure and 180 °C for 120 mins. After curing, the CFRP plates were cut into the DCB substrate with dimensions: 205 × 25 × 1 mm^3 (length × width × height). Then, on the smooth side of the substrate, the surface was carefully sanded with 360-grit sandpaper in a criss-cross pattern and cleaned with a soaked acetone tissue. The spider silk-inspired overlapping curl (OC) structures were manufactured using commercial polyamide filament, primarily composed of Polyamide 6 (PA6, F3 PA Pure Pro), obtained from Fiberthree GmbH (Darmstadt, Germany). The PA6 material exhibits high ductility (fracture strain > 200 %) [31], making it suitable for bridging reinforcements by enabling a longer effective bridging length. The bi-component epoxy adhesive Araldite 2015-1, supplied by Huntsman International LLC, was used to secondary bond the CFRP substrates.

2.2. 3D-printing of two-array, two-dimensional overlapping curl mesh

The OC filaments containing coiling fibers with sacrificial bonds and hidden lengths were fabricated using a Prusa i3 MK3S+ 3D printer equipped with a 0.15 mm nozzle. Fig. 1(b) shows the schematic of the 3D-printing process. The nozzle temperature was set to 225 °C, while the printing bed temperature was maintained at 40 °C. To induce the liquid rope coiling (LRC) effect [32], molten PA6 was extruded from the nozzle at a volumetric flow speed of $E = 25$ mm/min onto the printing bed from a nozzle height of $h = 3$ mm. Simultaneously, the nozzle moved at a speed of $F = 250$ mm/min. Under these conditions, a single OC filament aligned along the y-direction was spontaneously formed through the LRC instability using a simple linear nozzle movement, rather than by prescribing a complex nozzle deposition path. To fabricate periodically spaced OC filaments, the nozzle was translated by 5 mm in the y-direction — see Fig. 1(b) and the printing process was repeated using identical parameters. This procedure ensured a uniform spacing of 5 mm between adjacent OC filaments, corresponding to a periodic characteristic wavelength of $\lambda = 5$ mm, defined as the center-to-center distance between neighboring filaments. After completing the first array (along the y-direction) of OC filaments, the nozzle movement direction was rotated by 90°, and the second array of OC filaments was printed along the x-direction while adopting the same strategy. Through this sequential process, a two-array, two-dimensional OC mesh reinforcement was fabricated as shown in Fig. 1(c). The selected 3D-printing parameters ensured stable fabrication of the OC mesh through the LRC process and were adopted as a representative configuration for investigating the proposed toughening mechanism. Table 1 summarizes the 3D-printing process parameters and geometries of the OC mesh.

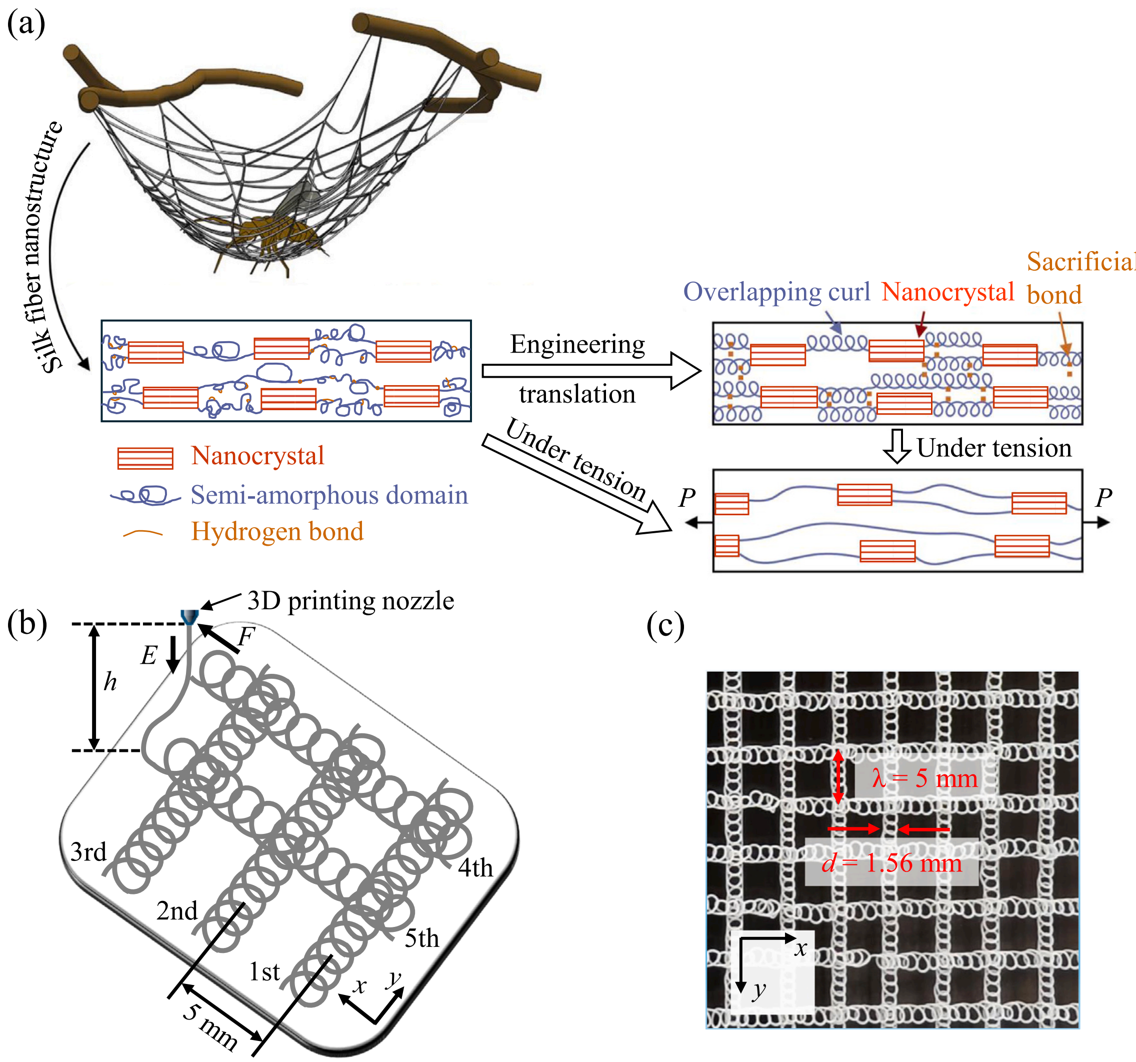

Fig. 1. (a) Energy absorption mechanisms in spider webs: fly capture and microscale toughening via sacrificial bonds and hidden lengths [28]. (b) The 3D-printing process schematic of OC mesh. The numbering (1st, 2nd, 3rd, ...) indicates the fabrication sequence of the OC filaments. (c) The spider web-inspired 3D-printed two-array, two-dimensional overlapping curl mesh reinforcement.

Table 1
3D-printing parameters for the overlapping curl mesh and obtained OC (mesh) geometries.

Printing parameters	Values	OC mesh geometries	Values (mm)
Nozzle diameter	0.15 mm	OC filament diameter	0.23 ± 0.015
Nozzle temperature	225 °C	OC curl diameter, *d*	1.56 ± 0.035
Printing bed temperature	40 °C	OC mesh characteristic wavelength, *λ*	5
Nozzle height	3 mm	OC mesh thickness	0.98 ± 0.027
Filament extrusion speed	25 mm/min		
Nozzle moving speed	250 mm/min		

2.3. DCB specimens manufacturing

The previously printed two-array OC mesh was cut into rectangular specimens with dimensions of approximately 60 × 20 mm (length in the *x*-direction × width in the *y*-direction) and used as inserted reinforcement, as illustrated in Fig. 2. Prior to integration into the adhesive, the OC mesh was coated with a layer of release agent to reduce surface adhesion.

The OC mesh comprises two printed arrays: the bottom array is aligned along the *x*-direction (x-oriented OCs), while the top array is aligned along the *y*-direction (y-oriented OCs). Two mesh orientation configurations were considered: one aligned the x-oriented OCs with the crack propagation direction (0mesh) and the other rotated by 45° relative to the crack path (45mesh). Following the approach proposed in [24], strips of non-sticky Teflon tape were intentionally attached to the surface of the OC mesh in a bottom-up alternating manner to create predefined adhesion patterned regions. Owing to their non-bonding surfaces, the tape inserts locally suppressed adhesive bonding, thereby introducing designed low-adhesion regions within the bondline. During crack propagation, these regions promoted controlled interfacial delamination, guided crack propagation, and facilitated hidden length bridging by the OC reinforcement. The spacing between adjacent tapes was 5 mm, equal to the tape width. Two tape orientations were considered: tapes aligned parallel to the *x*-direction (0tape) and tapes

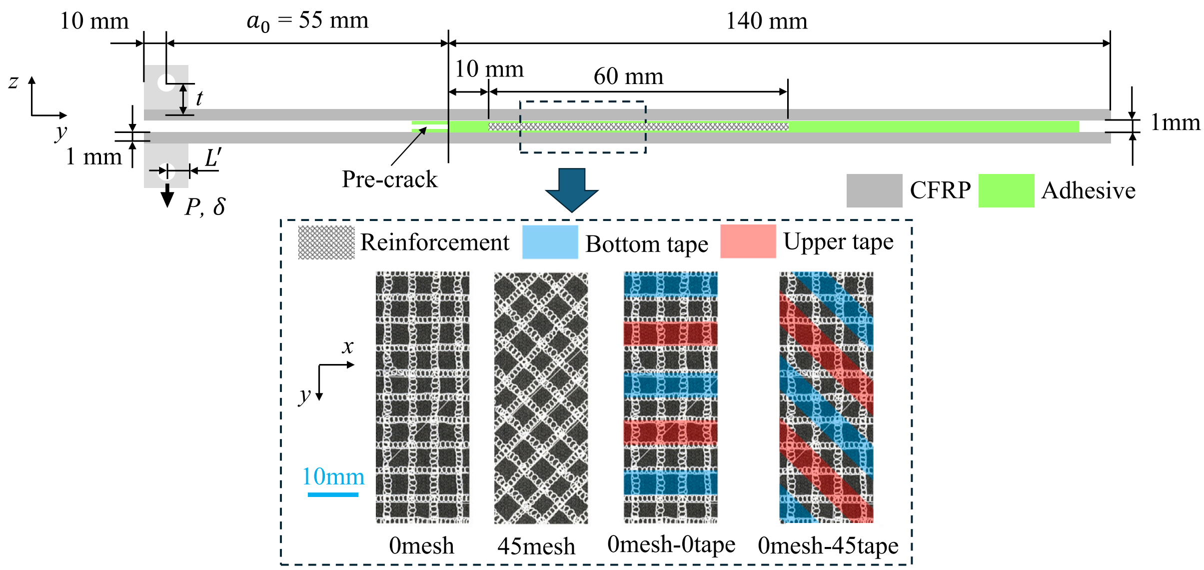

Nomenclature	0mesh	45mesh	0mesh-0tape	0mesh-45tape
Bondline area (mm^2)	1500	1500	1500	1500
OC mesh area (mm^2)	516.92	497.69	258.46	240.79
OC mesh coverage	0.34	0.33	0.17	0.16

Fig. 2. Schematic of the double cantilever beam specimen with an OC mesh reinforcement embedded within the adhesive bondline. For the OC mesh configuration, "0" denotes an orientation of 0° with respect to the x-direction for the OC filaments or adhesion tape, while "45" denotes an orientation of 45° with respect to the x-direction. The OC mesh coverage in the bondline are listed in the table, which is defined as the ratio of the area occupied by the OC mesh reinforcement to the bondline area: $\frac{\text{OC mesh area}}{\text{Bondline area}}$.

oriented at 45° (45tape). By maintaining the same OC mesh while varying only the tape orientation, the influence of adhesion patterning could be distinguished from that of mesh orientation. Accordingly, four reinforcement configurations were investigated: 0mesh (reference without adhesion patterning), 45mesh (effect of mesh orientation), 0mesh–0tape (effect of adhesion patterning), and 0mesh–45tape (effect of adhesion patterning orientation), as illustrated in Fig. 2.

The OC mesh coverage was defined as the ratio of the OC mesh area to the total bondline area, as summarized in the inset table of Fig. 2. The DCB-0mesh and DCB-45mesh specimens exhibited nearly identical OC mesh coverages (0.34 and 0.33, respectively), while the corresponding values for the DCB-0mesh-0tape and DCB-0mesh-45tape specimens were reduced to 0.17 and 0.16, owing to the introduction of adhesion-patterned regions. This approximately 50 % reduction indicates that a substantial portion of the OC reinforcement was intentionally left unbonded.

For the fabrication of the DCB specimens, the surfaces of the CFRP substrates were first treated using an in-house UV/ozone apparatus for 7 min, as recommended in [5,33]. Spacers with a thickness of 1 mm were attached to both ends of the substrates to precisely control the bondline thickness. In addition, a sharp razor blade was inserted into one end of the bondline prior to curing to create the pre-crack, resulting in the initial unbonded region shown in Fig. 2. Subsequently, the adhesive (Araldite 2015-1) was applied onto the bottom CFRP substrate. The OC mesh reinforcement was then carefully positioned onto the adhesive layer, with its leading edge located 10 mm ahead of the initial crack front to allow stable crack initiation and propagation before interaction with the reinforcement. Finally, the upper CFRP substrate was placed on top. Additional weights were applied to impose a uniform mechanical pressure, ensuring intimate contact between all interfaces. Finally, the assembled DCB specimens were cured in an oven at 80 °C for 1 h to complete the adhesive curing process. Reference specimens using pure Araldite 2015-1 adhesive were also prepared for comparison. The geometry of the DCB sample is shown in Fig. 2.

2.4. DCB test

A Zwick electro-mechanical testing machine equipped with a 1 kN load cell was used to conduct quasi-static mode I DCB tests. The tests were performed at a constant crosshead displacement rate of 2 mm/min, in accordance with ASTM D5528 [34]. For each DCB configuration, at least five specimens were tested. The experimental setup is shown in Fig. 3. During testing, crack propagation was monitored using a front-view camera. A millimeter scale marked on the side surface of each specimen was used as the reference for manually identifying the crack tip position and measuring the crack length throughout the test. In addition, a traveling microscope was employed to record side-view images of the fracture process, enabling detailed visualization of crack morphology and fracture mechanisms. Both imaging systems were synchronized with the load and displacement data acquired from the testing machine and automatically captured images every four seconds.

The energy release rate (ERR) of the DCB specimen was calculated based on the compliance calibration data reduction method [34]:

$$\mathrm{ERR} = \frac{nP\delta}{2Ba} \cdot \frac{F}{N} \tag{1}$$

where P is the load and δ is the displacement recorded during the DCB testing. B is the specimen width, a is the crack length, n is the exponent of the slope between $log(C/N)$ and $log(a_i)$, where $C = \delta_i/P_i$. Although manual crack-tip identification introduces a small measurement uncertainty, the calibration exponent n is determined from a least-squares fit of the $log(C/N) - log(a)$ relationship, thereby minimizing its influence on the calculated ERR. The correction factors F and N, accounting for the effects of large specimen deflection and loading-block geometry, respectively, are given by:

$$F = 1 - \frac{3}{10}(\frac{\delta}{a})^2 - \frac{3}{2}(\frac{\delta t}{a^2}) \tag{2}$$

$$N = 1 - (\frac{L'}{a})^3 - \frac{9}{8}[1 - (\frac{L'}{a})^2](\frac{\delta t}{a^2}) - \frac{9}{35}(\frac{\delta}{a})^2 \tag{3}$$

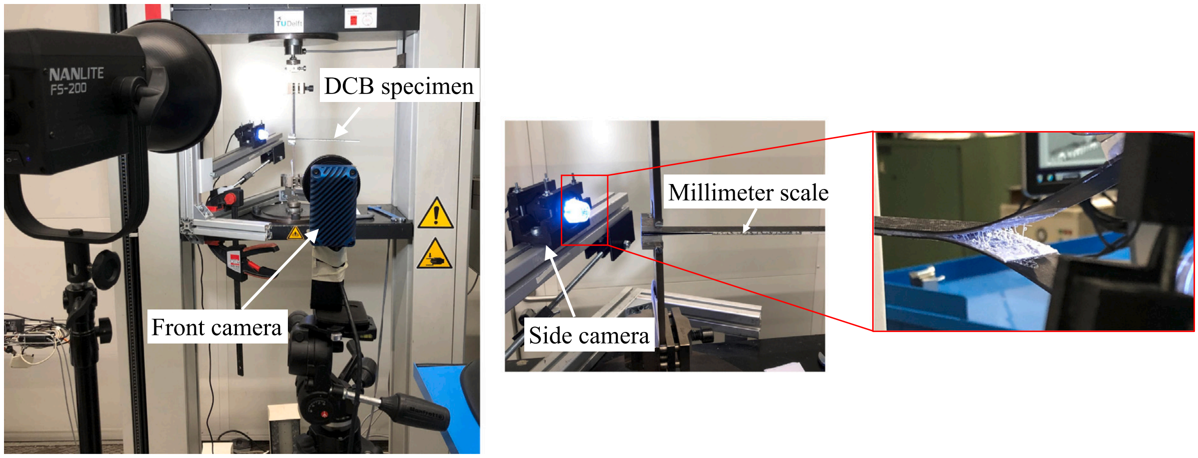

Fig. 3. Mechanical setup for DCB testing.

where L' is the horizontal distance between center of the loading pin and edge of the loading block ($L' = 5\,\text{mm}$), while t is the vertical distance between the center of the loading pin and the mid-plane of the substrate ($t = 10\,\text{mm}$). According to ASTM D5528, the contribution of F becomes particularly important when the opening displacement-to-crack length ratio (δ/a) exceeds 0.4 [34]. Since the OC mesh reinforcement produces substantial crack opening displacements during crack propagation, all ERR values reported in this study were calculated using the corrected ASTM formulation.

2.5. X-ray micro-computed tomography

X-ray micro-computed tomography (X-ray CT, CoreTOM, TESCAN, Belgium) was employed for ex-situ observation of the DCB samples. Before scanning, the DCB samples were loaded to a certain crack length, then the substrate openings were fixed by carefully inserting a metallic spacer to keep opening displacement for the ex-situ observations. The X-ray source was powered by a voltage of 110 kV and a target power of 15 W with 2856 × 2856 pixels flat panel detector. The scanning consisted of 3439 projections at a measuring time of 125 ms per single image with a voxel size of 15 μm. Once the 2D images were acquired, the 3D volume reconstruction was carried out on Panthera 1.6.4 software. 3D volumes were visualized through the commercial software Avizo (Avizo, Thermo Fisher Scientific, Massachusetts, USA).

3. Results

3.1. OC mesh reinforcements without adhesion patterning

Fig. 4 presents the DCB test results for the integrated OC mesh without adhesion patterning, including (a1, b1) load–displacement, (a2, b2) crack length–displacement, and (a3, b3) energy release rate curves. The DCB-Pure results, corresponding to specimens without reinforcement mesh, are also plotted as references. From the load–displacement curves, both the DCB-0mesh and DCB-45mesh specimens exhibit higher load levels than the DCB-Pure specimen after a certain opening displacement (about 40 mm for the DCB-0mesh and 30 mm for the DCB-45mesh). In addition, the crack length–displacement curves indicate that, for a given crack length, the OC mesh–reinforced specimens require a larger opening displacement of the CFRP substrates to sustain crack propagation, after a certain value of opening displacement. This behavior demonstrates that the presence of the OC mesh effectively delays crack growth. Consistently, the corresponding ERR curves show an increase in ERR with crack advance for both mesh configurations. For each specimen, ERR_{ini} was defined as the initial calculated ERR corresponding to the onset of stable crack propagation, whereas ERR_{max} was defined as the maximum ERR attained during crack propagation. Over the entire crack propagation process, the DCB-0mesh specimen exhibits a total ERR improvement of $\Delta\text{ERR} = \text{ERR}_{max} - \text{ERR}_{ini} = 0.35\,\text{kJ/m}^2$ (34 % improvement) relative to its initial value, whereas a larger improvement of $\Delta\text{ERR} = 0.56\,\text{kJ/m}^2$ (47 % improvement) is achieved for the DCB-45mesh specimen. Moreover, the ratio $\Delta\text{ERR}/\Delta a$, representing the average ERR increase per unit crack extension, is also greater for the DCB-45mesh configuration ($10.2\,\text{kJ/m}^3$), indicating a more effective toughening response. A summary of the ERR results for the OC mesh–reinforced composite adhesively joints is provided in Table 2.

Table 2
Summary of obtained ERR values of DCB samples with different reinforcements (average ± standard deviation). ERR_{ini}: initial energy release rate at the onset of crack propagation; ERR_{max}: maximum energy release rate measured during crack propagation. $\Delta\text{ERR} = \text{ERR}_{max} - \text{ERR}_{ini}$.

Nomenclature	ERR_{ini} (kJ/m^2)	ERR_{max} (kJ/m^2)	ΔERR (kJ/m^2)
0mesh	0.97 ± 0.10	1.30 ± 0.08	0.33 ± 0.02
45mesh	0.95 ± 0.18	1.40 ± 0.22	0.45 ± 0.10
0mesh-0tape	0.70 ± 0.09	0.87 ± 0.07	0.16 ± 0.13
0mesh-45tape	0.76 ± 0.07	0.97 ± 0.14	0.21 ± 0.070

Representative loading stages corresponding to the maximum ERR are selected in Fig. 5(a) and (b) to compare the ERR enhancement and the differences between the 0mesh and 45mesh configurations. The in-situ images reveal that the integrated OC mesh activates a substantial amount of filament bridging in both cases, with bridging filaments distributed continuously over a wide region, thereby contributing to the observed ERR improvement. Although filament bridging is clearly observed in both configurations, direct comparison based solely on the DCB experimental images remains difficult because of the large number and complex spatial distribution of the activated filaments. Moreover, the apparent amount of bridging observed from the images cannot directly explain the difference in ERR improvement between the two configurations. Therefore, fracture surface profiles, shown beneath the corresponding experimental images, are further analyzed to quantitatively evaluate the extent of effective OC bridging. On the fracture surfaces, OC curls extracted from the adhesive and participating in effective bridging are identified and highlighted in blue. These activated regions directly contribute to crack bridging and the associated ERR enhancement, whereas the remaining portions of the integrated OC mesh that do not participate in bridging are excluded from the analysis. To enable a quantitative comparison between different OC mesh geometries, the activated OC bridging area ratio is defined as

$$\eta = \frac{A_b}{A_{\text{mesh}}}, \tag{4}$$

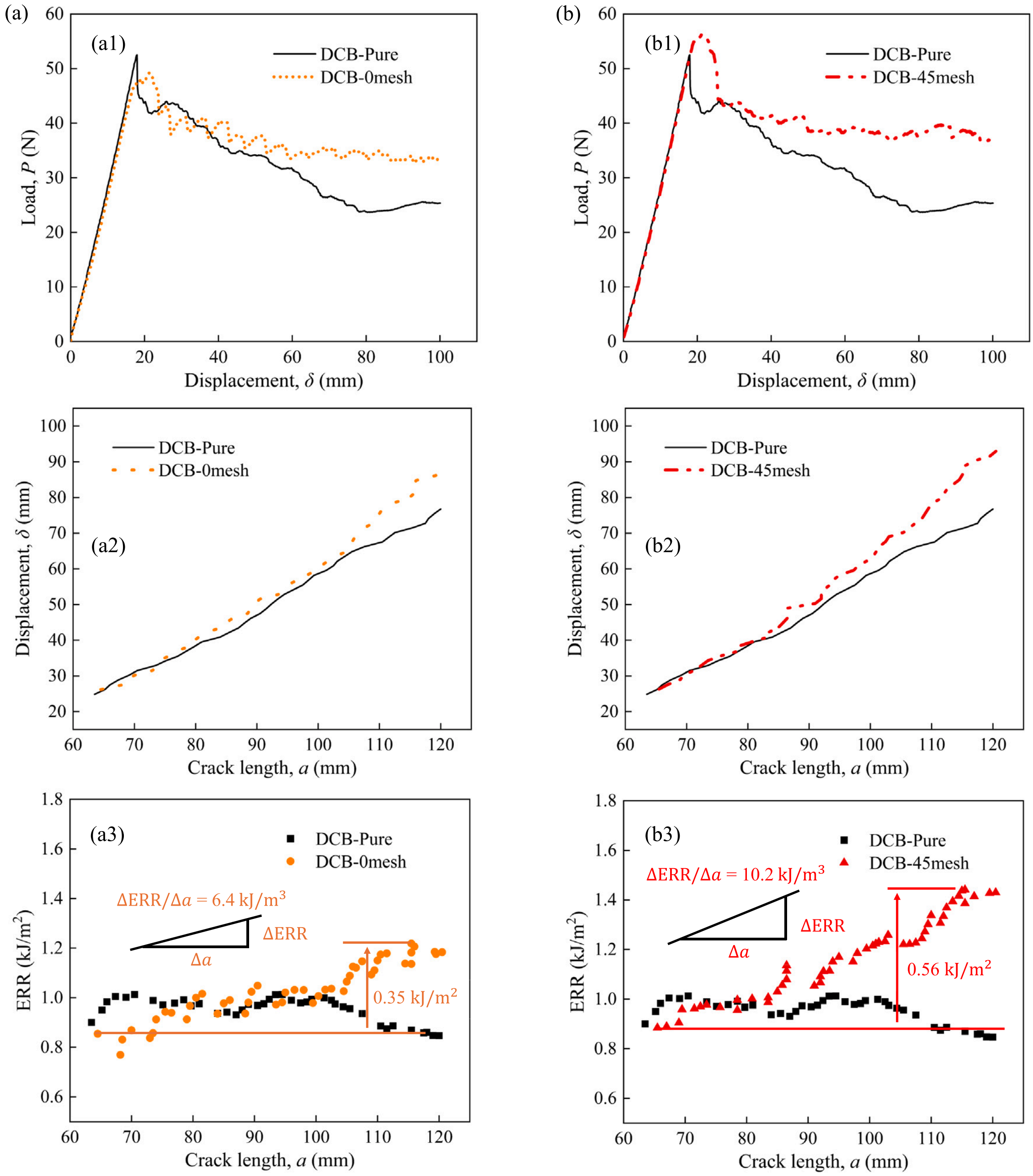

Fig. 4. Typical DCB experimental results for the (a) DCB-0mesh and (b) DCB-45mesh specimens, including (a1, b1) load–displacement, (a2, b2) crack length–displacement, and (a3, b3) energy release rate curves. The DCB-Pure specimen is included for comparison.

where A_b denotes the area of the activated OC bridging filaments, determined from the highlighted blue regions, and $A_{mesh} = 60 \times 20 = 1200\,\text{mm}^2$ is the total area of the integrated OC mesh. This ratio definition provides a more direct measure of OC filament bridging activation in the 2D mesh architecture.

The calculated values of η are presented in Fig. 5(c). The DCB-45mesh specimen exhibits a higher η value than the DCB-0mesh specimen, indicating that more OC bridging filaments are activated in the 45°-oriented OC mesh. This enhanced bridging activation is consistent with the greater ERR improvement observed for the DCB-45mesh configuration. However, the OC mesh coverages of the DCB-0mesh (0.34) and DCB-45mesh (0.33) specimens are comparable (see the inset table in Fig. 2), indicating that reinforcement coverage alone is insufficient to explain the observed toughening performance. Instead, reinforcement orientation governs the activation of filament bridging and, consequently, the enhancement in fracture resistance.

3.2. OC 0°-mesh with 0°-adhesion patterning

Fig. 6 shows the typical (a) load–displacement, (b) experimental process, (c) crack-displacement, and (d) energy release rate curves of DCB-0mesh-0tape sample. The DCB-Pure results are also plotted as references. Fig. 6(c) and (d) are deliberately arranged in the same column so that they share a common crack-length axis.

As shown in Fig. 6(a), pronounced stick–slip behavior is observed in the DCB-0mesh-0tape specimen with increasing displacement. Correspondingly, Fig. 6(c) shows a stepwise evolution of crack length with displacement, as indicated by the vertical dashed lines. The corresponding ERR curve in Fig. 6(d) exhibits periodic rising–dropping features. The fracture surfaces shown beneath the figure correlate well with the measured crack lengths. The spacing between successive minima in the ERR curve closely matches that between adjacent inserted tapes,

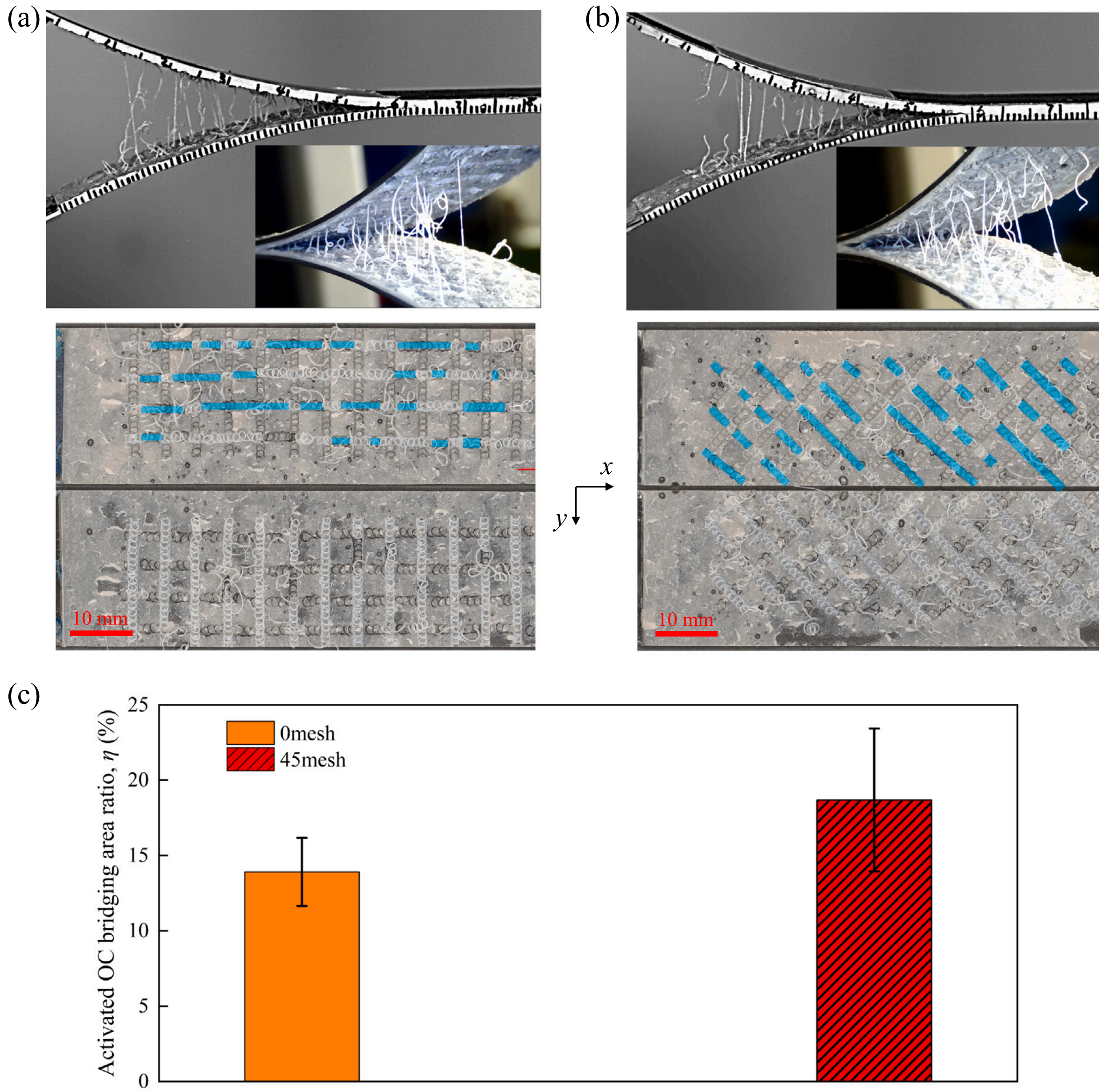

Fig. 5. Experimental process pictures at maximum ERR and fracture surfaces of (a) DCB-0mesh and (b) DCB-45mesh samples. (c) The activated OC bridging area ratio, η. In the captured experimental process pictures, the main image is obtained from the front camera, while the inset shows the side-camera view. (For interpretation of the references to color in this figure legend, the reader is referred to the web version of this article.)

indicating that this periodic behavior is governed by the 0°-oriented adhesion patterning. It should be noted that the crack length is measured from the specimen side edge and therefore does not exactly represent the crack-front position at the mid-plane. As a result, the peak ERR values do not precisely coincide with the tape termination locations. Nevertheless, the clear periodic trend in the ERR curve provides strong evidence that the introduced adhesion patterning effectively induces crack path deflection and the associated stick–slip behavior.

In Fig. 6(d), the initial ERR of the DCB-0mesh-0tape specimen is lower than that of the DCB-Pure specimen. This reduction is possibly attributed to the locally weakened interface introduced by the adhesion patterning. However, we still observe a rising trend in the ERR with the crack advance. Fig. 6(b) presents combined images of the crack propagation process captured by the front and side cameras. Starting from the selected point ②, (also indicated in Fig. 6(d)), several OC bridging filaments are clearly activated. As the crack propagates further toward point ③, an increasing number of bridging OC filaments is activated, leading to enhanced crack tip shielding and corresponding to the contribution of the maximum ERR improvement ($0.26\,\mathrm{kJ/m^2}$). Notably, no OC bridging is observed within the 0°-adhesion patterning regions, which are highlighted by blue markers in the front-view images of the DCB-sample, indicating that the adhesion patterning locally suppresses overlapping curl bridging activation.

3.3. OC 0°-mesh with 45°-adhesion patterning

As shown in the load–displacement curve of the DCB-0mesh-45tape specimen in Fig. 7(a), a notable difference compared with the DCB-0mesh-0tape specimen is the absence of stick–slip behavior. Instead, relative to the DCB-Pure specimen, a broad load-drop region is observed over the displacement range of 20–50 mm, followed by a gradual increase in load that eventually exceeds that of the DCB-Pure specimen (after approximately 60 mm opening displacement). Consistently, the ERR curve in Fig. 7(d) does not exhibit the characteristic rise–drop behavior; rather, a relatively stable but lower ERR plateau is observed over the crack length range of $a = 65$ mm to 88 mm. This distinct fracture behavior can be interpreted from the crack propagation mechanism shown in Fig. 7(b)-point ①. As the crack enters the 45°-oriented

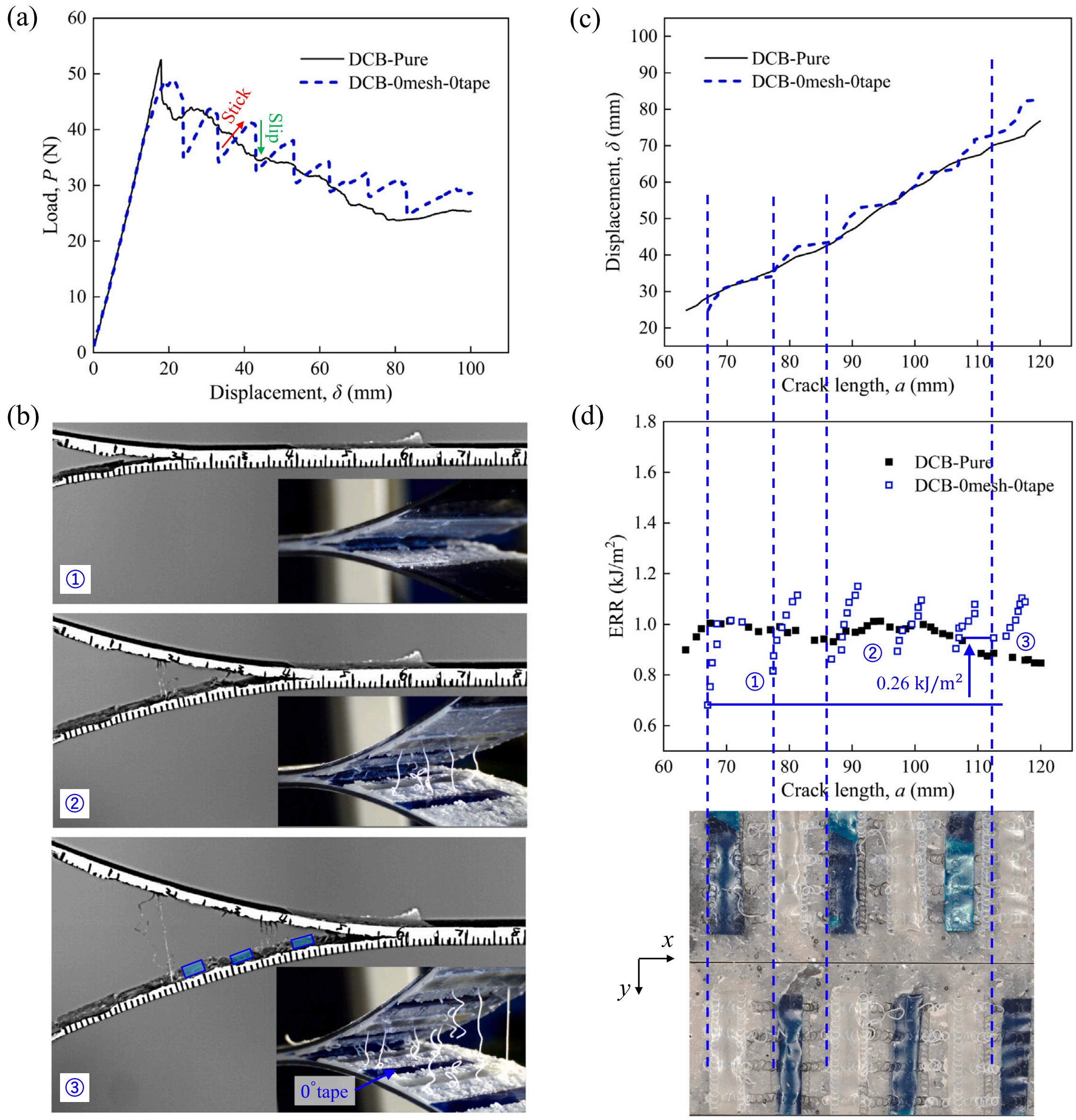

Fig. 6. Typical (a) load–displacement curves, (b) experimental process images captured by the front camera with the side camera view shown in the inset, (c) crack length–displacement curves, and (d) energy release rate curves for the DCB-0mesh-0tape specimens. The DCB-Pure specimen is included as a reference. (For interpretation of the references to color in this figure legend, the reader is referred to the web version of this article.)

adhesion-patterned region, the inclined weak interface prevents the crack front from spanning the entire patterned zone instantaneously, in contrast to the 0°-oriented case. Instead, the crack advances progressively along the inclined path, as indicated by the red arrow. Consequently, during crack propagation, part of the adhesive layer has already fractured (pink dashed arrow), while other regions remain intact and have not yet been reached by the advancing crack front. This asynchronous crack advance suppresses the stick–slip behavior. Meanwhile, the 45°-oriented patterning covers a wider weakened region along the crack path, distributing low adhesion over a larger area. As a result, the energy release process becomes more gradual, leading to a wider but lower ERR plateau compared to the DCB-Pure specimen.

Despite this adhesion patterning-induced weakening, the ERR increases progressively with crack advance, ultimately reaching an enhancement up to 0.28 kJ/m^2 (point ③) toward the end of crack propagation. At point ③ in Fig. 7(b), a greater number of OC bridging filaments is activated compared with the DCB-0mesh-0tape specimen. This increased activation of OC bridging compensates for the weakening effect introduced by the 45°-oriented adhesion patterning, resulting in an ERR improvement driven by the increased contribution of filament bridging effect.

In summary, the OC mesh reinforcement without adhesion patterning activates a greater number of bridging filaments compared to configurations with adhesion patterning. In addition, both the mesh orientation and the adhesion-patterning orientation play a critical role in governing the extent of OC bridging activation and the resulting ERR enhancement. The underlying mechanisms responsible for these observations are further discussed in the following sections.

4. Discussion

4.1. Orientation effect on triggering OC bridging mechanism

4.1.1. Orientation-dependent OC bridging mechanisms in OC mesh without patterning adhesion

Based on the experimental results presented in Section 3.1, the orientation of the OC mesh is assumed to induce distinct crack front

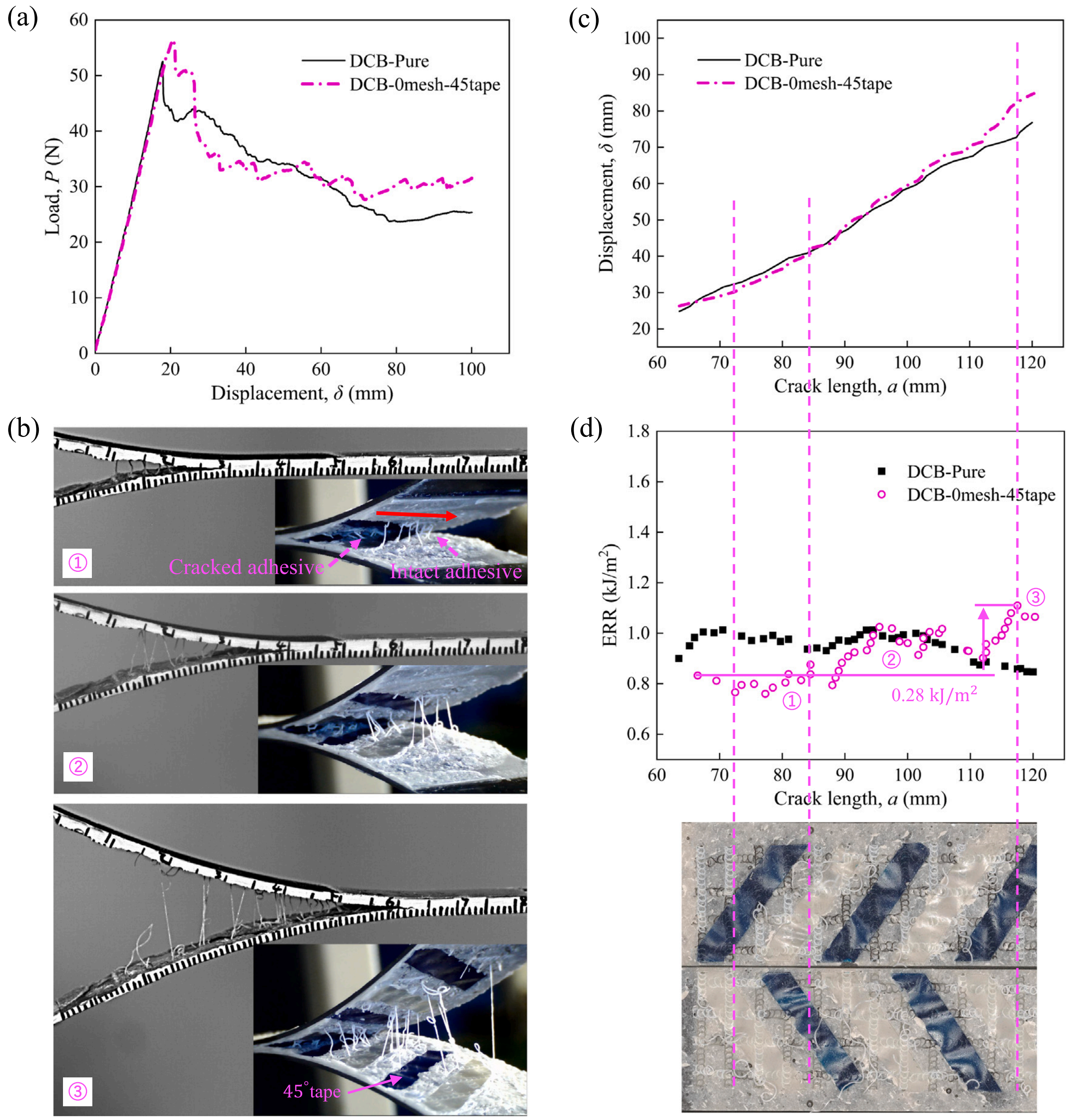

Fig. 7. Typical (a) load–displacement curves, (b) experimental process images captured by the front camera with the side-camera view shown in the inset, (c) crack length–displacement curves, and (d) energy release rate curves for the DCB-0mesh-45tape specimens. The DCB-Pure specimen is included as a reference. (For interpretation of the references to color in this figure legend, the reader is referred to the web version of this article.)

morphologies and propagation behaviors, which influence the activation of OC bridging. However, these features cannot be fully captured by in-situ optical observations or post-mortem fracture surface analysis alone. To address this limitation, X-ray CT was employed to non-destructively visualize crack front evolution and reveal its three-dimensional characteristics. Fig. 8(a) presents three-dimensional X-ray CT reconstructions of the DCB-0mesh specimen at a fixed crack length. The longitudinal-section view are defined by the xy-sectional plane indicated by the white arrow along the crack propagation direction. Fig. 8(b) and (c) present longitudinal X-ray CT views of DCB specimens reinforced with 0° and 45° OC mesh configurations, respectively. In these images, the white regions correspond to the intact adhesive, whereas the dark regions represent the crack front. The integrated OC mesh appears as a continuous dark curly pattern.

For the DCB-0mesh specimen (Fig. 8(b)), the crack front, highlighted by red solid lines, exhibits approximately rectilinear morphologies. The red dashed rectangle further reveals localized crack dispersion in the vicinity of the y-oriented bottom-array OC filaments, indicating a strong interaction between the crack path and the mesh architecture. This behavior can be attributed to the weak interfacial boundary between the OC mesh and the adhesive. The mesh reinforcement is fabricated from PA6, which has inherently low surface adhesion, and is further coated with a release agent prior to integration. As a result, the crack preferentially propagates along the mesh–adhesive interface, forming adhesion-patterned paths aligned with the OC geometry, which guide the crack front into a uniform, rectilinear configuration following the y-oriented OCs. In contrast, the DCB-45mesh specimen shown in Fig. 8(c) exhibits a pronounced zig-zag crack-front morphology, as delineated by the red solid lines. This zig-zag pattern closely follows the architecture of the 45°-oriented OC mesh. Within the region highlighted by the red dashed rectangle, the crack front propagates along inclined paths at approximately 45°, guided and constrained by the boundaries defined by adjacent OC filaments. The red arrows further indicate discontinuous or jumped crack tip positions occurring in the regions between neighboring filaments, reflecting the influence of the 45°-oriented reinforcement on the crack propagation behavior. Moreover, the fracture surface topology was quantitatively characterized using the

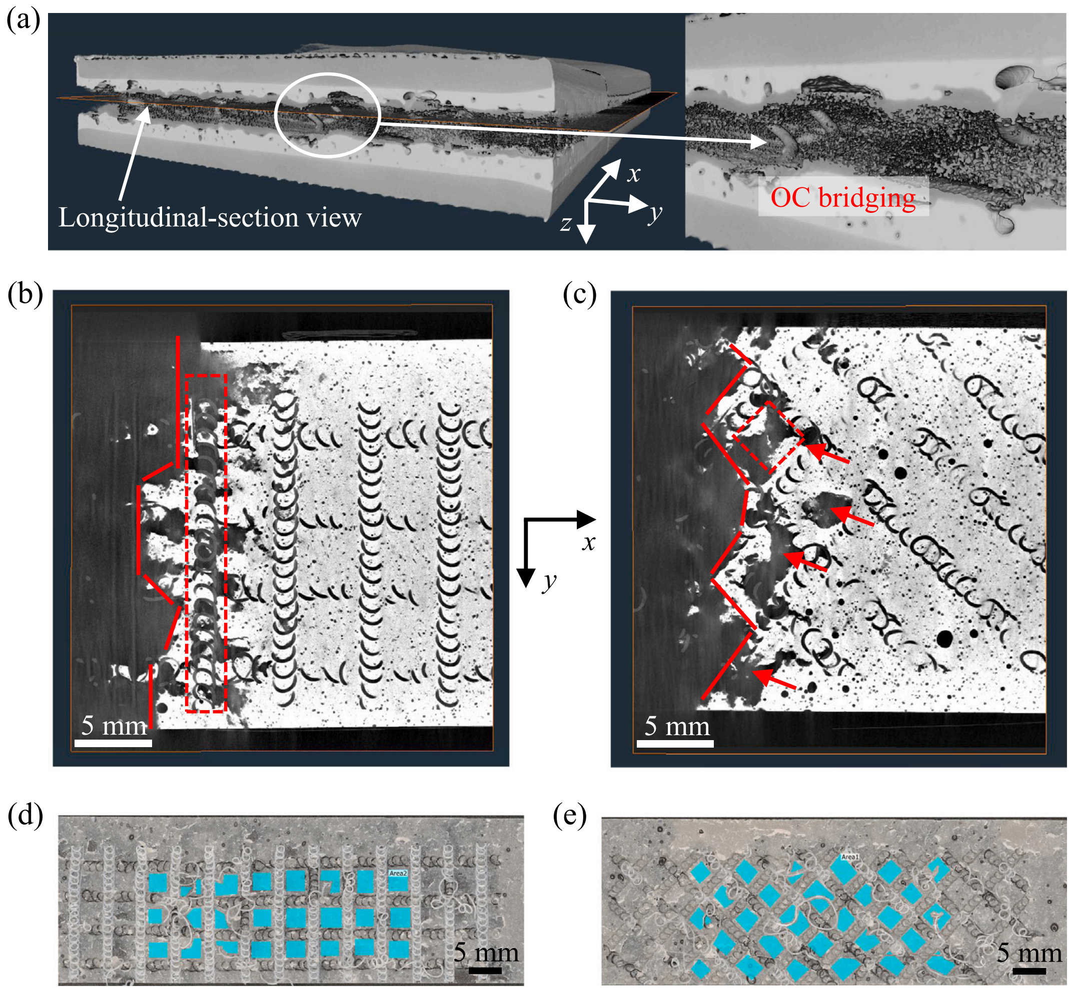

Fig. 8. (a) X-ray CT scan images of DCB-0mesh sample at a fixed crack length with defined longitudinal-section view. Longitudinal-section views of the crack front in (b) 0mesh and (c) 45mesh integrated DCB specimens. The white region represents the adhesive, while the dark region corresponds to the crack front. The integrated OC mesh forms the continuous dark curly pattern. The red lines delineate the crack-front profiles. The red arrows and dashed rectangles highlight the jumped crack-tip locations. Representative fracture surface highlighted regions of Sdr measurements for the (d) DCB-0mesh and (e) DCB-45mesh samples, respectively. The measurement regions were extracted excluding the OC filaments and their surface imprints. (For interpretation of the references to color in this figure legend, the reader is referred to the web version of this article.)

developed interfacial area ratio (Sdr), which represents the percentage increase in the true three-dimensional fracture surface area relative to its projected area. The measurement regions are highlighted in Fig. 8(d) and (e), excluding the OC filaments and their surface imprints. The Sdr value increased from 0.13 for the DCB-0mesh to 0.29 for the DCB-45mesh, indicating that the 45°-oriented mesh configuration generated additional fracture surface area compared to the 0°-oriented mesh. This quantitative result is consistent with the X-ray CT observations of enhanced crack deflection, bifurcation, and a more tortuous crack path. The non-uniform crack front morphology also has implications for the interpretation of the measured fracture resistance. The R-curves were calculated using the measured crack length according to the ASTM D5528 [34] data reduction procedure. Since the crack length was monitored from the specimen side, the measured crack length represents the average crack extension rather than the local crack front morphology. Consequently, the calculated R-curves should be interpreted as the apparent global fracture resistance. Although local crack front undulations and stick–slip propagation may influence the instantaneous fracture process, these effects are inherently reflected in the measured load–displacement response and therefore do not compromise the relative comparison among different reinforcement configurations.

Beyond the mesh orientation investigated in this study, other geometric parameters such as filament spacing, curl geometry, and mesh density are also expected to influence crack–reinforcement interaction and bridging activation by altering the probability of crack engagement and the available hidden length. A systematic optimization of these geometric parameters is beyond the scope of the present work and will be addressed in future studies.

4.1.2. Orientation-dependent OC bridging mechanisms in OC mesh with patterning adhesion

Fig. 9(a) and (b) present longitudinal views along the crack propagation direction for DCB specimens with OC mesh and adhesion patterning. For the DCB-0mesh-0tape specimen (Fig. 9(a)), the crack front exhibits a regular and uniform morphology aligned with the boundaries of the adhesion-patterned regions, as marked by the dark-white contrast and indicated by the yellow dashed lines. In Fig. 9(b), the DCB-0mesh-45tape specimen shows a distinct crack-front segmentation, outlined by yellow dashed lines, arising from the 45°-oriented adhesion patterning. The crack front in the lower portion of the section is clearly delayed relative to that in the upper patterned region, indicating non-uniform crack advance. Moreover, the crack propagates into the regions between adjacent patterned zones (red arrow 1), while simultaneously deviating toward the y-oriented OC filaments

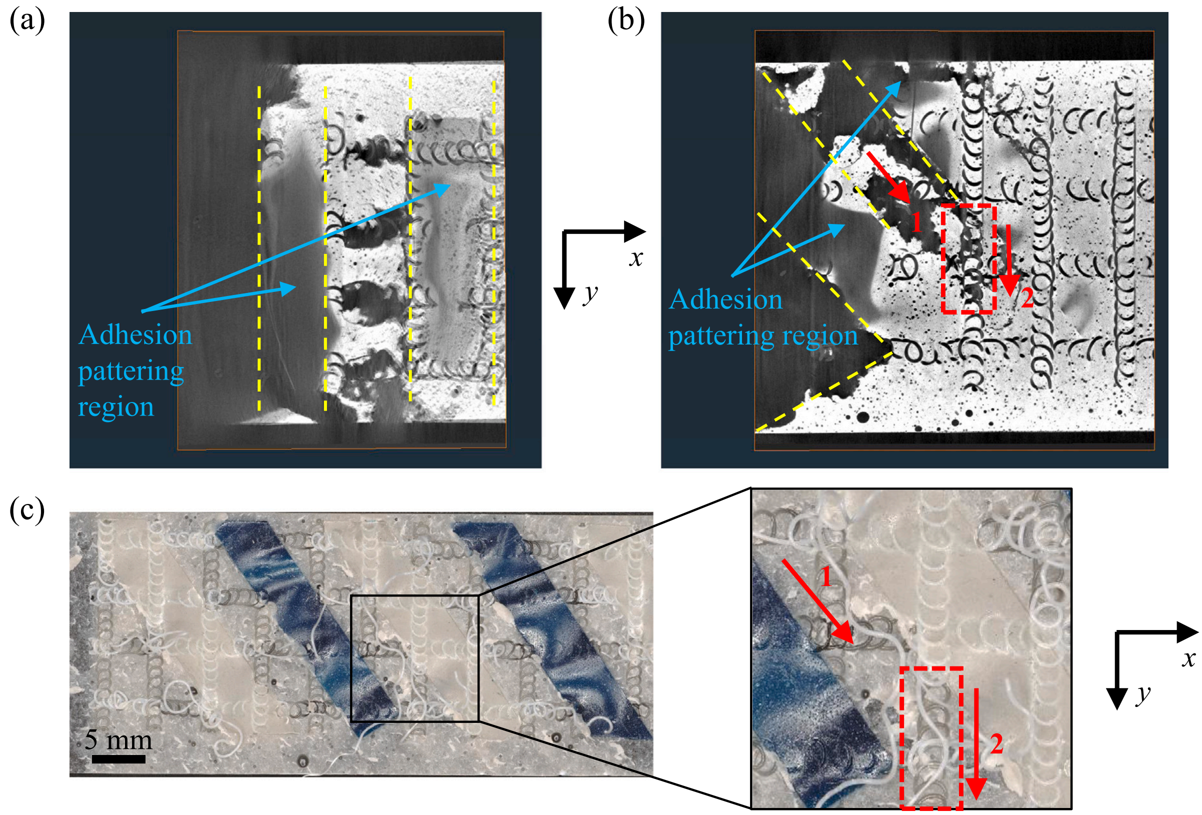

Fig. 9. Transverse-section views of the crack propagation front of (a) DCB-0mesh-0tape and (b) DCB-0mesh-45tape samples. (c) Fracture surface of DCB-0mesh-45tape sample. The red arrows indicate the deflected crack front and the red dashed rectangle highlights the triggered y-oriented OC filaments. (For interpretation of the references to color in this figure legend, the reader is referred to the web version of this article.)

(red arrow 2). This deflection promotes bridging from the y-oriented OCs (highlighted by the red dashed rectangle), as confirmed by the zoomed fracture surface inset in Fig. 9(c). The increased participation of y-oriented filaments is consistent with the greater extent of OC bridging observed in the DCB-0mesh-45tape specimen compared to the DCB-0mesh-0tape specimen, as observed in Figs. 6(b) and 7(b).

In conclusion, X-ray CT observations demonstrate that the integrated OC mesh introduces spatially distributed interfacial heterogeneity aligned with its architecture, thereby effectively guiding crack propagation. In contrast, for specimens with adhesion patterning, the crack front largely follows the predefined patterned geometry. Moreover, both mesh orientation and adhesion-patterning orientation strongly influence crack-front morphology. In particular, the 45°-oriented OC mesh induces a zig-zag crack front, which promotes more pronounced crack deflection and bifurcation than the 0°-oriented configuration, thereby enhancing the activation of OC bridging. These mechanisms are quantitatively supported by the in-situ observations and the evaluated OC bridging ratio η (Fig. 5), where the 45°-oriented OC mesh exhibits a higher η, confirming a greater extent of filament activation.

4.2. Competition between adhesion patterning and OC mesh surface topography in triggering OC bridging

4.2.1. Intrinsic adhesion patterning induced by OC mesh geometric topology

Fig. 10(a) shows the fracture surface of the DCB-0mesh-0tape specimen, which exhibits minimal OC bridging. As highlighted in the inset, the fracture surface within the tape-covered region appears smooth and glossy. In this region, the OC mesh is fully embedded in the adhesive and the OC curls (i.e., hidden lengths) are completely filled. The infilled adhesive acts as obstacles, suppressing the activation of OC bridging. Consequently, the 0°-oriented adhesion patterning inhibits effective bridging in this configuration. In contrast, Fig. 10(b1) shows the fracture surface of the DCB-0mesh specimen, where extensive OC bridging is observed. Most y-oriented OCs remain embedded within the adhesive, contributing little to bridging, whereas the x-oriented OCs dominate the initiation and sustained development of bridging. Side-view images of the 0° OC mesh (Fig. 10(b2)) show that the y-oriented OCs form the bottom array, with flattened lower surfaces resulting from adhesion to the printing bed during fabrication, while the x-oriented OCs are deposited on top. This stacked filament-array arrangement produces local height variations at overlapped regions and reduced height between adjacent filaments, resulting in an inherently wavy surface morphology analogous to the engineered waviness reported by Yudhanto et al. [23]. Such geometric irregularity, together with the low-adhesion mesh–adhesive interface, promotes preferential crack propagation along the mesh surface topology and induces crack deflection, as illustrated in Fig. 10(b3). This intrinsic architectural effect effectively mimics adhesion patterning and facilitates the activation of OC bridging.

4.2.2. Deformation zone length

Both the non-sticky tapes and the OC mesh itself can introduce adhesion-patterning effects; however, their effectiveness in triggering OC bridging differs significantly, as evidenced by the comparison between the DCB-0mesh-0tape and DCB-0mesh specimens. This contrast indicates distinct crack–reinforcement interaction mechanisms and motivates further analysis to elucidate the key factors governing bridging activation.

From our previous study [24], it was indicated that when the adhesion patterning width is close to the deformation zone length of the joint, it is easier to guide the crack propagation path through the adhesion patterning. To quantify this length scale, the deformation zone

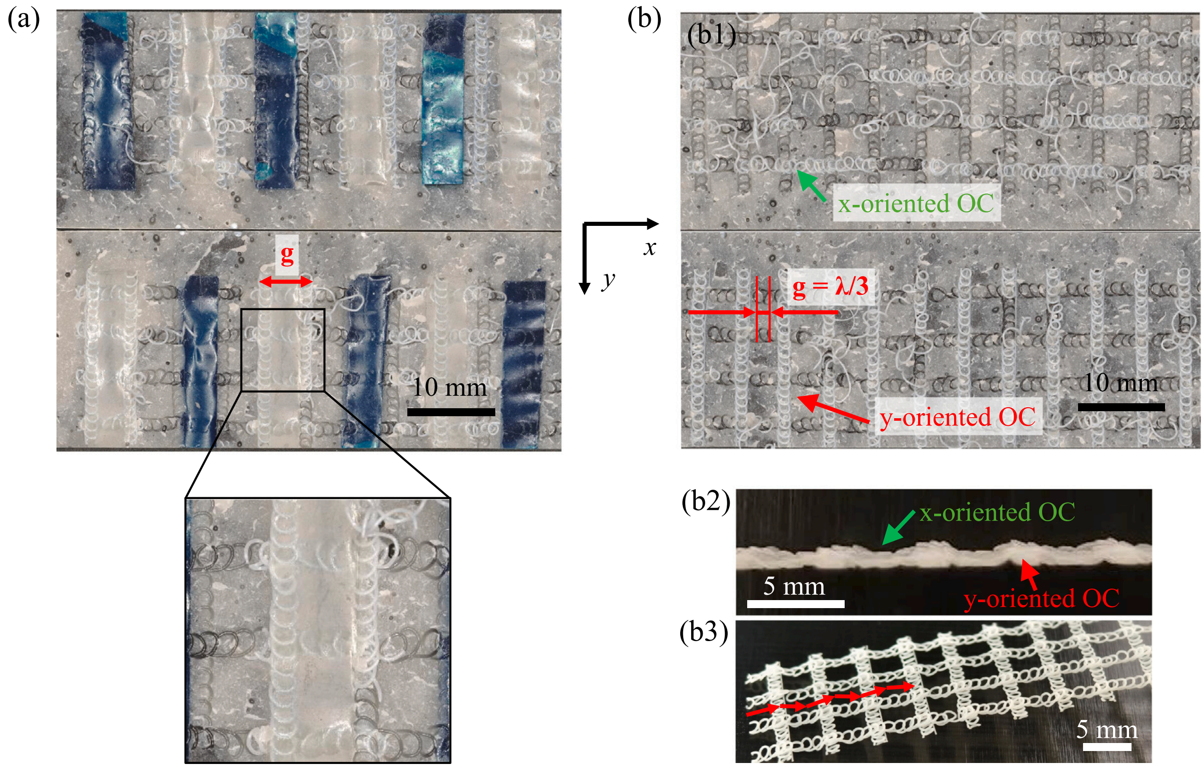

Fig. 10. (a) Fracture surface of DCB-0mesh-0tape. (b) Fracture surface of DCB-0mesh and the side views of the 0°-OC mesh reinforcement configuration. The red arrows in (b3) indicate the potential crack propagation path. (For interpretation of the references to color in this figure legend, the reader is referred to the web version of this article.)

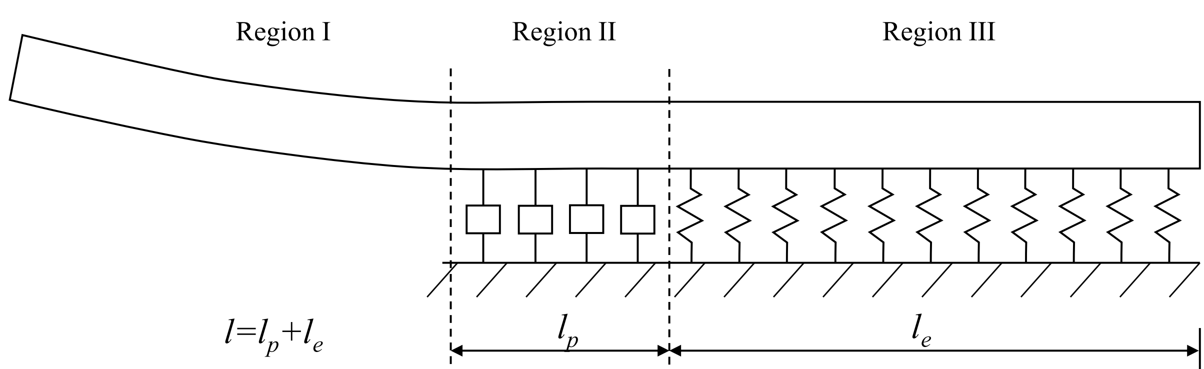

Fig. 11. Schematic illustration of the deformation zone in DCB joint based on elastic–plastic foundation theory [24,35].

ahead of the crack tip is evaluated using an elastic–plastic foundation model for the DCB configuration, following the framework proposed by S. E. Yamada [24,35], as illustrated in Fig. 11. Owing to symmetry about the adhesive mid-plane, the DCB arm can be divided into three distinct regions. Region I corresponds to the free segment subjected to the opening load. Region II represents the plastic zone, where the adherends are supported by a perfectly plastic foundation due to adhesive yielding, characterized by a plastic process zone length l_p. Region III denotes the elastic zone, in which the adherends are supported by an elastic foundation with a characteristic length l_e.

The plastic process zone length l_p is estimated based on the fracture behavior of the bulk adhesive under plane strain conditions [36]:

$$l_p = \frac{1}{6\pi}\frac{E_a G_{Ia}}{\sigma_y^2}\frac{1}{(1-\nu_a^2)} \tag{5}$$

where E_a is the adhesive Young's modulus, G_{Ia} is the mode I fracture toughness, σ_y is the yield stress, and ν_a is the Poisson's ratio of the adhesive.

In the elastic region, the foundation stiffness k is given by [37]:

$$k = 2m_q\frac{E_a b}{t_a} \tag{6}$$

with

$$m_q = \frac{1-\nu_a}{(1-2\nu_a)(1+\nu_a)} \tag{7}$$

under plane strain conditions, where t_a denotes the adhesive thickness. The elastic process zone length is defined as $l_e = \lambda^{-1}$, where λ satisfies:

$$\lambda^4 = \frac{k}{4E_x^{sub} I} \tag{8}$$

Here, E_x^{sub} is the longitudinal Young's modulus of the substrate and $I = bh^3/12$ is the second moment of inertia of the DCB arm, with h being its thickness. Substituting k and expanding I yields [37]:

$$\lambda^4 = 6m_q\frac{E_a}{E_x^{sub}}\frac{1}{t_a h^3} \tag{9}$$

Using material properties reported for Araldite 2015-1 adhesive [38], namely $E_a = 1790\,\text{MPa}$, $\sigma_y = 16.17\,\text{MPa}$, and $\nu_a = 0.4$, together with substrate properties $E_x^{sub} = 161\,000\,\text{MPa}$ [39] and $h = 1\,\text{mm}$, and taking $t_a = 1\,\text{mm}$ and $G_{Ia} = 0.95\,\text{kJ/m}^2$, the plastic and elastic process zone lengths are estimated as $l_p = 0.41\,\text{mm}$ and $l_e = 1.89\,\text{mm}$, respectively. The total deformation zone length of the studied DCB joint is therefore $l = 2.3\,\text{mm}$.

In the 0mesh–0tape reinforcement, the adhesion patterning width g is equal to the non-sticky tape width of 5 mm, as marked on the fracture surface in Fig. 10(a). For the OC mesh itself (without adhesion patterning), the "adhesion-patterning effect" is not externally imposed but arises intrinsically from the mesh geometry and surface morphology. As shown in Fig. 10(b2) and (b3), crack propagation preferentially follows the mesh–adhesive interface, where the periodic OC curls continuously alter the local crack propagation direction. Within the spacing of a single curl, the crack path remains approximately unchanged; however, when the crack front reaches the adjacent curl, the wavy surface morphology induces a local crack deflection. Therefore, each curl effectively acts as an individual crack-guiding unit and the spacing between adjacent curls can be regarded as the characteristic adhesion patterning width governing local crack deviation. For the 0°-oriented mesh, approximately three curls are distributed within one wavelength $\lambda = 5\,\text{mm}$, giving an average curl spacing of $\lambda/3 \approx 1.67\,\text{mm}$. This value is therefore taken as the effective adhesion-patterning width associated with the OC mesh. Compared with the 0mesh–0tape configuration ($g = 5\,\text{mm}$), this characteristic width is closer to the deformation zone length, resulting in more effective crack guidance and a greater activation of bridging filaments [24].

4.3. Design guidelines for OC mesh reinforcement configuration

A detailed comparison between the 0mesh and 45mesh configurations (both of which exhibit significant OC bridging) reveals that the activated bridging area factor satisfies $\eta_{45\text{mesh}}/\eta_{0\text{mesh}} = 1.34$, determined from the fracture surface analysis in Fig. 5(c). Consistently, the ratio of the maximum ERR enhancement, calculated from Table 2, is $\Delta\text{ERR}_{45\text{mesh}}/\Delta\text{ERR}_{0\text{mesh}} = 1.36$. The close agreement between these two ratios indicates that the observed ERR improvement in OC mesh–reinforced CFRP joints is predominantly governed by the OC bridging mechanism.

The apparent ERR measured from OC mesh–reinforced composite joints can be decomposed into intrinsic and extrinsic contributions, as expressed in Eq. (10). The term ERR_0 represents the intrinsic energy dissipation at the crack front, while $\text{ERR}^{\text{bridging}}(g,\theta,\eta,m)$ denotes the extrinsic energy dissipation arising from OC bridging. This bridging contribution is controlled by the combined effects of the reinforcement adhesion patterning width g, the orientation of the mesh and adhesion patterning θ, the amount of activated OC bridging quantified by η, and the material properties m of the reinforcement filaments:

$$\text{ERR}_{\text{appa}} = \text{ERR}_0 + \text{ERR}^{\text{bridging}}_{(g,\theta,\eta,m)} \tag{10}$$

From a reinforcement design perspective, the adhesion patterning width g and orientation θ must be carefully tailored to promote crack deflection and crack front bifurcation, thereby maximizing the activation of OC bridging filaments (i.e., increasing η). Fig. 12(a) presents a design–fracture performance map that synthesizes the experimental findings into a practical design guideline for OC mesh reinforcement. The reinforcement orientation, θ, is plotted against the maximum energy release rate improvement, ΔERR, while the dimensionless parameter $\frac{g}{l}$ (adhesion-patterning width normalized by the deformation zone length) is represented by the color scale. For a given $\frac{g}{l}$, the largest ERR enhancement is obtained when the reinforcement orientation (e.g., 45°) is misaligned with the crack propagation direction. Moreover, for a fixed θ, the ERR improvement increases as $\frac{g}{l}$ approaches 1, i.e., when the adhesion-patterning width matches the deformation zone length. Since the ERR enhancement is dominated by OC bridging, the design map reveals that the activated bridging area ratio η is governed by the reinforcement geometry. In particular, η can be expressed as a function of key geometric parameters, $\eta \propto f(g,\theta)$, highlighting the role of reinforcement architecture in controlling bridging activation and the resulting fracture resistance.

As schematically illustrated in Fig. 12(b), varying the OC mesh orientation ($\theta \in [0°, 90°]$) alters the crack front morphology from a idealized planar crack front to a more tortuous configuration. This trend is consistent with the experimental observations in Fig. 8(b), where the 45°-oriented mesh produces a pronounced zig-zag crack front. Such crack-front modulation is expected to influence both the effective crack-front length and the activation of OC bridging filaments, thereby affecting the overall fracture response [40]. However, the relative contributions of crack front geometry and filament bridging cannot be resolved from the present experiments alone. Future numerical simulations incorporating orientation-dependent crack propagation and bridging effects could provide further insight into the coupling between reinforcement orientation, crack front evolution, and bridging activation, enabling more systematic optimization of the OC mesh architecture.

In addition, the achievable toughening effect is also influenced by the load-carrying capacity of individual OC filaments; therefore, stronger filament materials (such as continuous carbon fiber reinforced PA6 material) may further enhance the contribution of the bridging mechanism.

Although the proposed OC mesh reinforcement significantly improves the mode I fracture toughness of bonded CFRP joints, several limitations should be acknowledged. First, the present study was conducted using laboratory-scale DCB specimens, and the scalability of the reinforcement strategy for larger bonded structures requires further investigation. Second, only one CFRP laminate configuration was considered. Different laminate configurations exhibit different bending stiffnesses, resulting in different crack opening displacements and, consequently, different levels of hidden length activation in the OC mesh. Therefore, the quantitative toughening effect may vary among composite structures. Finally, the present work focuses on quasi-static mode I loading. The applicability of the proposed reinforcement under mixed-mode, fatigue, and impact loading conditions remains to be investigated.

5. Conclusions

This work systematically investigated the extrinsic toughening mechanisms associated with filament bridging in bio-inspired overlapping curl mesh reinforced CFRP adhesively bonded joints under mode I loading. The 3D-printed two-array 2D OC mesh were integrated into the adhesive bondline with and without orientation-dependent adhesion patterning. A series of DCB specimens with different OC mesh orientations and adhesion patterning configurations was examined to elucidate the role of crack path guidance and OC filament bridging on the energy release rate. Based on the experimental results, fracture surface analyses, and X-ray CT observations, the following conclusions can be drawn:

- The combination of low interfacial adhesion and the two-array OC mesh architecture introduces inherent surface irregularity, which promotes crack deflection and activates extensive OC filament bridging, leading to enhanced ERR.
- The OC mesh orientation governs crack-front morphology. Compared with the rectilinear crack front in the 0°-oriented mesh, the 45°-oriented mesh induces a zig-zag crack front, enhancing crack deflection and bifurcation, and resulting in more efficient bridging and up to 47 % ERR improvement.
- Adhesion patterning facilitates crack deflection but may suppress bridging activation, particularly in the 0°-oriented configuration, leading to limited filament bridging.

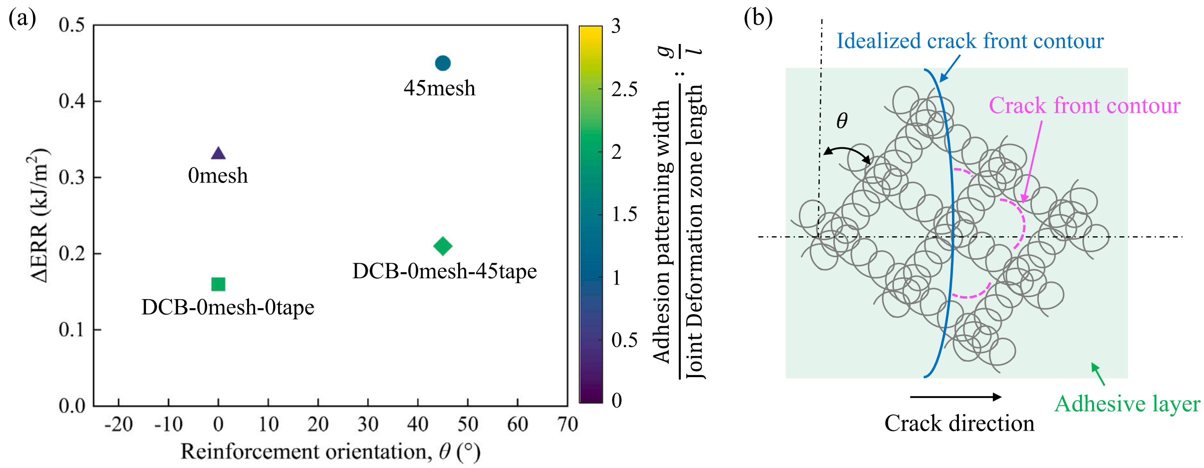

Fig. 12. (a) OC mesh reinforcement design–fracture performance map derived from the experimental results. (b) Definition of crack propagation and OC mesh reinforcement orientation in the adhesive layer. (For interpretation of the references to color in this figure legend, the reader is referred to the web version of this article.)

- The orientation of adhesion patterning plays a key role in crack evolution. The 45°-oriented pattern promotes crack-front bifurcation more effectively than the 0°-oriented pattern, thereby enhancing filament bridging activation.
- The activation of OC bridging and the associated ERR enhancement are governed by the coupled effects of adhesion patterning width, orientation, and filament material properties, highlighting the importance of crack–reinforcement interactions in extrinsic toughening.

Overall, integrating bio-inspired OC mesh reinforcements into adhesive bondlines provides an effective extrinsic toughening strategy for CFRP joints by guiding crack propagation and promoting filament bridging. Although the current performance is constrained by the load-bearing capacity of individual filaments, the mechanistic insights obtained here establish clear design principles for enhancing joint fracture resistance through optimized reinforcement architecture and material selection. To further facilitate practical engineering applications, future work will investigate the long-term durability of the proposed bio-inspired joints under environmental aging, including moisture absorption, thermal cycling, and their combined effects on interfacial stability and fracture performance.

CRediT authorship contribution statement

Zhiyuan Xu: Writing – original draft, Formal analysis, Data curation, Conceptualization. **Ran Tao:** Writing – review & editing, Supervision, Conceptualization. **Sofia Teixeira de Freitas:** Writing – review & editing, Supervision, Conceptualization.

Declaration of generative AI and AI-assisted technologies in the manuscript preparation process

During the preparation of this work the author(s) used ChatGPT in order to readability. After using this tool/service, the author(s) reviewed and edited the content as needed and take(s) full responsibility for the content of the published article.

Declaration of competing interest

The authors declare that they have no known competing financial interests or personal relationships that could have appeared to influence the work reported in this paper.

Acknowledgments

The authors gratefully acknowledge the financial support from the China Scholarship Council (No. CSC202107720061). This work is also supported by Fundacao para a Ciencia e a Tecnologia (FCT) for its financial support via LAETA (project https://doi.org/10.54499/UID/50022/2025).

Data availability

Data will be made available on request.

References

[1] Ravichandran B, Balasubramanian M. Joining methods for fiber reinforced polymer (FRP) composites- a critical review. Compos Part A: Appl Sci Manuf 2024;108394.
[2] Marques AC, Mocanu A, Tomić NZ, Balos S, Stammen E, Lundevall A, Abrahami ST, Günther R, de Kok JM, Teixeira de Freitas S. Review on adhesives and surface treatments for structural applications: Recent developments on sustainability and implementation for metal and composite substrates. Materials 2020;13(24):5590.
[3] Lima R, Tao R, Bernasconi A, Carboni M, Carrere N, De Freitas ST. Uncovering the toughening mechanisms of bonded joints through tailored CFRP layup. Compos Part B: Eng 2023;263:110853.
[4] Chu Y, Sun L, Zhan B, Yang X, Zhang C, Huang W. Static and dynamic behavior of unbalanced bonded joints with adhesion defects in automotive structures. Compos Struct 2019;226:111234.
[5] Tserpes K, Barroso-Caro A, Carraro PA, Beber VC, Floros I, Gamon W, Kozłowski M, Santandrea F, Shahverdi M, Skejić D, et al. A review on failure theories and simulation models for adhesive joints. J Adhes 2022;98(12):1855–915.
[6] van Innis C, Budzik MK, Pardoen T. Bridging in co-cured composite joints. Int J Solids Struct 2025;309:113194.
[7] Tao R, Li X, Yudhanto A, Alfano M, Lubineau G. Toughening adhesive joints through crack path engineering using integrated polyamide wires. Compos Part A: Appl Sci Manuf 2022;158:106954.
[8] Hu P, Pulungan D, Tao R, Lubineau G. Influence of curing processes on the development of fiber bridging during delamination in composite laminates. Compos Part A: Appl Sci Manuf 2021;149:106564.
[9] Rao Q, Ouyang Z, Peng X. Enhancing mode I fracture toughness of adhesively bonded unidirectional composite joints using surfactant-stabilized multi-walled carbon nanotube and graphene nanoplate. Polym Test 2021;96:107110.
[10] Suzuki T, Matsuzaki R, Todoroki A, Mizutani Y. Crack growth analysis of a composite/adhesive interface toughened by in-mold surface preparation. Int J Adhes Adhes 2013;42:36–43.
[11] Yukimoto Y, Matsuzaki R, Todoroki A. Effects of mixed-mode ratio and step-shaped micro pattern surface on crack-propagation resistance of carbon-fiber-reinforced plastic/adhesive interface. Compos Part A: Appl Sci Manuf 2015;69:139–49.

[12] Kupski J, De Freitas ST. Design of adhesively bonded lap joints with laminated CFRP adherends: Review, challenges and new opportunities for aerospace structures. Compos Struct 2021;268:113923.
[13] Wagih A, Tao R, Yudhanto A, Lubineau G. Improving mode II fracture toughness of secondary bonded joints using laser patterning of adherends. Compos Part A: Appl Sci Manuf 2020;134:105892.
[14] Tao R, Li X, Yudhanto A, Alfano M, Lubineau G. On controlling interfacial heterogeneity to trigger bridging in secondary bonded composite joints: An efficient strategy to introduce crack-arrest features. Compos Sci Technol 2020;188:107964.
[15] Tao R, Li X, Yudhanto A, Alfano M, Lubineau G. Laser-based interfacial patterning enables toughening of CFRP/epoxy joints through bridging of adhesive ligaments. Compos Part A: Appl Sci Manuf 2020;139:106094.
[16] Kadlec M, Růžek R, Bělskỳ P. Concurrent use of Z-pins for crack arrest and structural health monitoring in adhesive-bonded composite lap joints. Compos Sci Technol 2020;188:107967.
[17] Yudhanto A, Lubineau G, Ventura IA, Watanabe N, Iwahori Y, Hoshi H. Damage characteristics in 3D stitched composites with various stitch parameters under in-plane tension. Compos Part A: Appl Sci Manuf 2015;71:17–31.
[18] Delzendehrooy F, Ayatollahi M, Akhavan-Safar A, Da Silva L. Strength improvement of adhesively bonded single lap joints with date palm fibers: Effect of type, size, treatment method and density of fibers. Compos Part B: Eng 2020;188:107874.
[19] Quan D, Wang X, Pan J, Ma Y, Scarselli G, Zhao G. Enhancing the fracture toughness of aerospace-grade carbon fibre/epoxy composites by interlaying surface-activated low-melt polyaryletherketone (LMPAEK) meshes. Compos Part B: Eng 2024;287:111824.
[20] Quan D, Chen H, Qin L, Lin J, Dong G, Zhao G. Carbon fibre composite joints co-cured by advanced PEEK/PPS meshes with outstanding fracture toughness. Compos Sci Technol 2023;242:110200.
[21] Heide-Jørgensen S, de Freitas ST, Budzik MK. On the fracture behaviour of CFRP bonded joints under mode I loading: Effect of supporting carrier and interface contamination. Compos Sci Technol 2018;160:97–110.
[22] Maloney K, Fleck N. Toughening strategies in adhesive joints. Int J Solids Struct 2019;158:66–75.
[23] Yudhanto A, Almulhim M, Kamal F, Tao R, Fatta L, Alfano M, Lubineau G. Enhancement of fracture toughness in secondary bonded CFRP using hybrid thermoplastic/thermoset bondline architecture. Compos Sci Technol 2020;199:108346.
[24] Tao R, Xu Z, de Freitas ST. Mode I toughening of bio-based epoxy adhesive through 3D-printed biomimetic reinforcements. Compos Part B: Eng 2025;113313.
[25] Yang H, Wang Y, Jang Y, Shani K, Jiao Q, Peters M, Parker KK, Vlassak JJ. Biomimetic hierarchical fibrous hydrogels with high alignment and flaw insensitivity. Matter 2025;8(6).
[26] Chen S-M, Zhang Z-B, Gao H-L, Yu S-H. Bottom-up film-to-bulk assembly toward bioinspired bulk structural nanocomposites. Adv Mater 2024;36(23):2313443.
[27] Brunetta L, Craig CL. Spider silk: evolution and 400 million years of spinning, waiting, snagging, and mating (Yale University Press). 2010.
[28] Zou S, Therriault D, Gosselin FP. Spiderweb-inspired, transparent, impact-absorbing composite. Cell Rep Phys Sci 2020;1(11).
[29] Zou S, Therriault D, Gosselin FP. Toughening elastomers via microstructured thermoplastic fibers with sacrificial bonds and hidden lengths. Extrem Mech Lett 2021;43:101208.
[30] Xu Z, Tao R, Masania K, de Freitas ST. Bio-inspired overlapping curl structures for toughening bio-based epoxy: A study on the fracture phenomena. Compos Sci Technol 2025;111374.
[31] Xu Z, Tao R, Masania K, de Freitas ST. Biomimetic toughening design of 3D-printed polymeric structures: Enhancing toughness through sacrificial bonds and hidden lengths. Mater Des 2024;247:113361.
[32] Ribe NM, Habibi M, Bonn D. Liquid rope coiling. Annu Rev Fluid Mech 2012;44(1):249–66.
[33] Teixeira de Freitas S, Zarouchas D, Poulis J. The use of acoustic emission and composite peel tests to detect weak adhesion in composite structures. J Adhes 2018;94(9):743–66.
[34] ASTM D5528. Standard test method for mode I interlaminar fracture toughness of unidirectional fiber-reinforced polymer matrix composites. 2013.
[35] Yamada SE. Elastic/plastic fracture analysis for bonded joints. Eng Fract Mech 1987;27(3):315–28.
[36] Kin Loch A, Shaw S. The fracture resistance of a toughened epoxy adhesive. J Adhes 1981;12(1):59–77.
[37] Fernandes RL, Budzik MK, Benedictus R, de Freitas ST. Multi-material adhesive joints with thick bond-lines: Crack onset and crack deflection. Compos Struct 2021;266:113687.
[38] Fernandes RL, de Freitas ST, Budzik MK, Poulis JA, Benedictus R. From thin to extra-thick adhesive layer thicknesses: Fracture of bonded joints under mode I loading conditions. Eng Fract Mech 2019;218:106607.
[39] Gan KW, Hallett SR, Wisnom MR. Measurement and modelling of interlaminar shear strength enhancement under moderate through-thickness compression. Compos Part A: Appl Sci Manuf 2013;49:18–25.
[40] Hu P, Budzik MK. Designed intermittency in interlaminar fracture via kirigami-induced crack-front widening. Compos Sci Technol 2026;111611.